



COMMUNICATIONS PHYSICS

ARTICLE

<https://doi.org/10.1038/s42005-020-00412-3>

OPEN



Nanobenders as efficient piezoelectric actuators for widely tunable nanophotonics at CMOS-level voltages

Wentao Jiang^{1,2}, Felix M. Mayor^{1,2}, Rishi N. Patel¹, Timothy P. McKenna¹, Christopher J. Sarabalis¹ & Amir H. Safavi-Naeini¹✉

Tuning and reconfiguring of nanophotonic components are needed to realize systems incorporating many components. The electrostatic force can deform a structure and tune its optical response. Despite the success of electrostatic actuators, they suffer from trade-offs between tuning voltage, tuning range, and on-chip area. Piezoelectric actuation could resolve these challenges, but only pm-per-volt scale wavelength tunability has been achieved. Here we propose and demonstrate compact piezoelectric actuators, called nanobenders, that transduce tens of nanometers per volt. By leveraging the non-uniform electric field from submicron electrodes, we generate bending of a piezoelectric nanobeam. Combined with a sliced photonic crystal cavity to sense displacement, we show tuning of an optical resonance by $\sim 5 \text{ nm V}^{-1}$ (0.6 THz V^{-1}) and between $1520 \sim 1560 \text{ nm}$ (~ 400 linewidths) within 4 V. Finally, we consider tunable nanophotonic components enabled by the nanobenders.

¹ Department of Applied Physics and Ginzton Laboratory, Stanford University, 348 Via Pueblo Mall, Stanford, CA 94305, USA. ²These authors contributed equally: Wentao Jiang, Felix M. Mayor. ✉email: safavi@stanford.edu

Complete and low-power control over the phase and amplitude of light fields remains a major challenge in integrated photonics. Optical components providing such control are essential in systems being developed for optical computing, signal processing, sensing, and imaging^{1–3}. Tuning the optical response of an element entails changing its refractive index by, for example, modifying its temperature, imposing electric fields, or mechanically deforming it. Among these, mechanical deformations have the advantage of being essentially lossless, requiring no static power consumption, and possessing an enormous tuning range and cryogenic compatibility^{4,5}. Nano-opto-electromechanical (NOEM) devices^{4,6} have thus been pursued and demonstrated, to realize switches and couplers for classical and quantum light^{7–12}, resonant and static electro-optomechanical tuning and electro-optical transduction^{13–19}.

An efficient NOEM device solves two problems simultaneously. It is an optical device whose properties are exceptionally sensitive to mechanical deformations. It is also an electro-mechanical device where a modest voltage can induce large deformations. State-of-the-art optomechanical cavities routinely achieve coupling coefficients $g_{\text{OM}}/2\pi$ in excess of 100 GHz nm^{-1} , and largely satisfy the former requirement. It is more-so the latter requirement of large voltage-induced displacement, which has remained a formidable challenge in this context. Here, two approaches present themselves: electrostatic and piezoelectric forces. Electrostatic forces are generated by the voltage-induced polarization in a material. They do not require any special material property and have been previously used to implement a variety of NOEM systems. However, electrostatic actuation is limited by some combination of trade-offs between actuation range, sensitivity, device footprint, and speed. For example, we can increase the sensitivity by realizing a larger capacitor, but this comes at the cost of speed and footprint. Alternatively, the sensitivity can be increased by using smaller capacitor gaps, which then reduce the range of motion possible. In this work, we show how manifestation of the piezoelectric effect in a nanostructure can be used to realize transducers with capabilities beyond the range/footprint/speed/sensitivity trade-off present in electrostatic

devices. In the context of piezo-photonic integration, our work follows several efforts^{20–23} to implement piezo-optomechanically tunable cavities and waveguides which have resulted, for example, in demonstrations of cavity wavelength tuning coefficients ranging from 0.1 to 30 pm V⁻¹^{21–23}.

By considering the interplay between non-uniform electric fields and transverse components of the piezoelectric tensor \mathbf{d} , we discover an actuation mechanism specific to nanoscale piezoelectric actuators that leads to a two order of magnitude increase in achievable displacements. We propose and demonstrate a compact ($\sim 10 \mu\text{m}^2$) and geometrically isolated actuator, which we call a “nanobender”, composed of monolithic metal electrodes on a single layer of a thin-film piezoelectric. The displacement of the nanobender scales quadratically with its length L and can be as large as 20 nm V^{-1} for $L \sim 20 \mu\text{m}$. The enormous sensitivity and tuning range achieved in these nanobenders allow us to achieve a significant breakthrough in NOEM performance. We demonstrate a “zipper” optomechanical cavity^{24,25} actuated by four nanobenders that deform the structure to tune the optical resonance wavelength by $\sim 5 \text{ nm V}^{-1}$. With a tuning speed approaching 1 MHz, and a tuning range of 60 nm with around 4 V, we show single-mode tuning across the full telecom C-band with low voltages accessible from complementary metal-oxide-semiconductor (CMOS) electronics. We further show that the displacement generated by the nanobenders is sufficiently large to “zip” and “unzip” the zipper cavity, reversibly manipulating the mechanical mode structure of nanomechanical resonators with switchable contact forces.

Results

Operating principle of a piezoelectric nanobender. Consider a slab of piezoelectric material sandwiched between two electrodes that are separated by a length L and have a potential difference of U (Fig. 1a). The piezoelectric property of a material is represented by its charge piezoelectricity tensor \mathbf{d} , a third-rank tensor that relates strain to electric field inside a material ($\mathbf{S} = \mathbf{d} \cdot \mathbf{E}$). The terms $d_{11(22,33)}$ (Voigt notation) couple S_{kk} to E_k , for $k = x, y, z$,

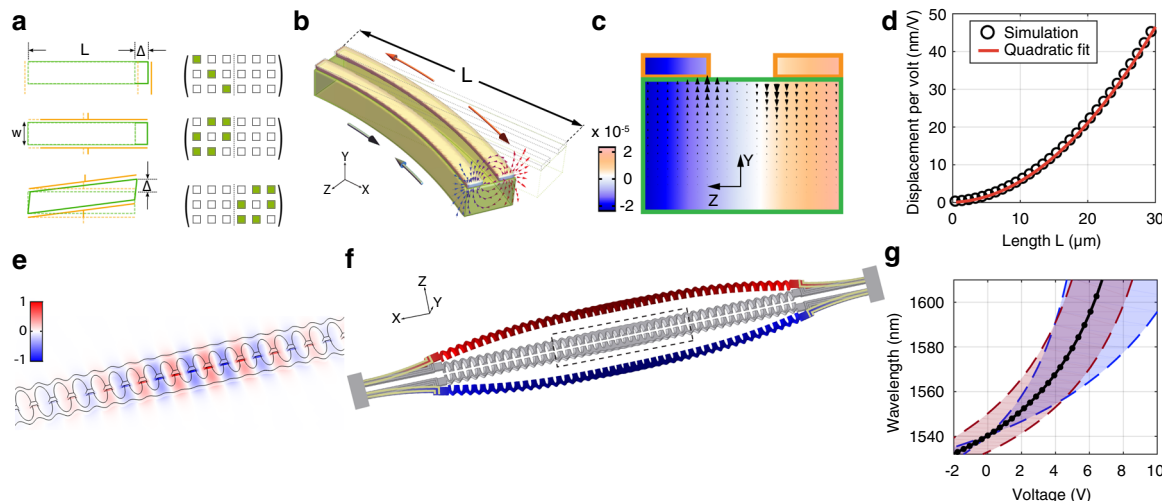


Fig. 1 The nanobender and tunable bender-zipper cavity design. **a** Schematic representation of how the components of the piezoelectric tensor affect the deformation of a beam (green) when a voltage is applied on electrodes (orange). **b** Visualization of a nanobender showing an applied electric field (small arrows), resulting strain (large arrows) and displacement of the fixed beam. **c** Cross-section of a nanobender showing the strain S_{XX} as well as the electric field E_Y (arrowheads) generated by the metal electrodes. **d** Simulated displacement at the tip of a nanobender as a function of its length. Notice the quadratic relationship. **e** Normalized E_Z component of the fundamental optical mode of the zipper cavity. **f** Displacement u_Z of the bender-zipper cavity with a voltage applied to four $L = 5 \mu\text{m}$ nanobenders. The deformation is amplified for illustration purposes. **g** Optical resonance wavelength versus voltage applied on a $L = 15 \mu\text{m}$ bender (black curve) for an initial gap of 203 nm. The blue region covers a bender length variation of $\pm 5 \mu\text{m}$. The red region covers initial gap sizes of $\pm 50 \text{ nm}$.

causing compressional/tensile strain to build up in the direction of the electric field. This leads to a displacement $\Delta = SL = d_{11}U$. Considering that $d \approx 10 \text{ pm V}^{-1}$ in standard piezoelectric materials such as aluminum nitride (AlN) and lithium niobate (LiNbO_3)^{26,27}, such a transducer would only generate displacements at the atomic scale for voltages $U \sim 1 \text{ V}$ which are easily produced by CMOS circuits.

The above expression $\Delta = d_{11}U$ also shows that the generated displacement does not depend on the size of the transducer. This applies to any piezoelectric actuator. We write the constitutive relation between the strain and the electric field $S = \mathbf{d} \cdot \mathbf{E}$, as $((\nabla \mathbf{u})^T + \nabla \mathbf{u})/2 = \mathbf{d} \cdot \nabla U$ where $\mathbf{u}(\mathbf{r})$ is the displacement field and $U(\mathbf{r})$ is the electric potential distribution for a given actuator geometry, applied voltage and boundary conditions. If the geometry of both the actuator and the boundary conditions are scaled by a factor ϵ while keeping the same applied voltage, then $\mathbf{u}'(\mathbf{r}) = \mathbf{u}(\mathbf{r}/\epsilon)$ and $U'(\mathbf{r}) = U(\mathbf{r}/\epsilon)$ are solutions to the new equations. In other words, the magnitude of the displacement stays constant as the actuator is shrunk leading to an increase in relative displacement that favors smaller actuators.

As illustrated above, the diagonal elements of \mathbf{d} , $d_{11(22,33)}$ give rise to tens of picometers of displacement at a potential of around one volt. A much larger displacement can be generated with transverse \mathbf{d} ($d_{12(13,23)}$) components (Fig. 1a). In this situation, the potential U gives rise to an electric field U/w across the width w , which generates strain along the length L of the beam. This leads to a displacement $\Delta \approx d \cdot UL/w \sim (0.01 \text{ nm V}^{-1}) \cdot RU$, where we have defined the aspect ratio of the actuator $\mathcal{R} \equiv L/w$. Compared to the previous case, the displacement is enhanced by \mathcal{R} . However, reaching $\Delta \sim 100 \text{ nm}$ with one volt still requires $\mathcal{R} = 10^4$, roughly on the same order as that of a long strand of human hair, or sheet of paper, making it impractical.

Is there a configuration that results in a displacement which scales faster than linear with \mathcal{R} ? Bending of a beam generates a displacement proportional to L^2 , where contraction occurs in one half of the beam and expansion in the other half. Looking back to the corresponding electric field E , we recognize that bending can be actuated by flipping the direction of E across the width of the beam. Assuming that the derivative of the E field is constant across the width of the beam $\partial_z E \sim U/w^2$ (z is transverse to the beam), the end-point displacement can be approximated by (Supplementary Note 1)

$$\Delta \approx \frac{1}{2} d \cdot \partial_z E \cdot L^2 \sim (0.01 \text{ nm V}^{-1}) \cdot \mathcal{R}^2 U. \quad (1)$$

We see that the displacement in this case is enhanced by the square of the aspect ratio \mathcal{R}^2 . The required \mathcal{R} for $\Delta \sim 100 \text{ nm}$ is drastically decreased to a practical value $\mathcal{R} = 100$. As an example, such a non-uniform E field on a $w \sim 400 \text{ nm}$ wide beam with length $L \sim 40 \mu\text{m}$ would enable actuation of 100 nm displacement per volt—a displacement on the same order as the width of the beam. We emphasize that the nanoscale aspect of the nanobender is important for achieving such a large relative displacement. By the scale-invariance arguments above, a larger structure would generate the same displacement, leading to a less appreciable relative motion.

A strongly inhomogeneous E field is naturally generated by the fringing fields of a submicron-scale electrode configuration. We consider a simple device, which we call the nanobender, where a pair of parallel electrodes lies on the top surface of a beam made of a thin piezoelectric LiNbO_3 film. For a beam oriented along the crystal axis X , the inhomogeneous E_Y field induces a varying strain S_{XX} and results in bending of the beam (Fig. 1b) via the piezoelectric tensor element d_{21} . For Y -cut LiNbO_3 where the crystal Y axis is perpendicular to the chip, this bending gives rise to an in-plane displacement that scales quadratically with L .

Finite-element simulations²⁸ of the nanobender are shown in Fig. 1c. The simulated E_Y (arrowheads) changes sign along Z , causing expansion in one half of the beam and contraction in the other. For all the simulations and experiments, we use a nanobender width $w = 450 \text{ nm}$, LiNbO_3 thickness $t = 300 \text{ nm}$, electrode width $w_m = 150 \text{ nm}$, electrode-electrode gap $w_g = 150 \text{ nm}$ and an aluminum electrode thickness $t_m = 50 \text{ nm}$. A more detailed study of how these parameters affect nanobender performance is presented in Supplementary Note 2. Once the nanobender's cross-section is fixed, the length L ultimately determines the maximum displacement Δ generated at the end of the beam. Through simulations (Fig. 1d) we are able to confirm the quadratic length-displacement relationship in equation (1). The simulated displacement along the other two directions are more than one order of magnitude smaller.

Actuation that induces bending is commonly adopted by macroscopic piezoelectric actuators, realizing displacement per volt values similar to the nanobenders ($\sim 0.1 \mu\text{m V}^{-1}$)²⁹. These structures can induce bending by utilizing multiple electrodes to switch the electric field direction, or multilayered piezoelectrics. Such approaches are possible in an integrated platform³⁰ but relatively difficult to realize, especially for in-plane actuation. Remarkably, electrostatic forces can also be used to generate bending with large travel³¹, though scaling actuators down to a few microns is challenging, and current demonstrations require much larger footprints for similar displacements ($\sim 50 \times 2000 \mu\text{m}^2$ for $\sim 0.1 \text{ nm V}^2$). Note that the flexoelectric effect, distinct from the piezoelectric effect, is also capable of generating bending from a homogeneous electric field^{32,33}. However, the piezoelectric effect in the nanobender exceeds the flexoelectric effect by orders of magnitude, which is thus neglected (see Supplementary Note 3 for estimates).

Integration with a zipper cavity. By integrating the nanobender with a nanophotonic “zipper” cavity^{24,25} on the thin-film LiNbO_3 material platform, we demonstrate its potential for realizing photonic devices with wide low-voltage tunability. A zipper cavity is a sliced photonic crystal consisting of two nano-patterned beams separated by a gap $\tilde{g}_0 \sim 200 \text{ nm}$ that confines an optical resonance. The E_Z component of the fundamental optical cavity mode is plotted in Fig. 1e. Due to the sub-wavelength confinement of the mode, the resonance wavelength of the cavity is strongly dependent on the gap between the two beams (Supplementary Note 4). A voltage applied to the nanobenders moves the two halves of the zipper cavity (Fig. 1f), tuning the optical resonance wavelength. In Fig. 1g we present the simulated voltage-wavelength tuning curve. The tuning curve is nonlinear due to the large changes in \tilde{g}_0 —a smaller \tilde{g}_0 increases the optical mode confinement and optomechanical coupling, increasing the slope of the tuning curve.

To couple light into the device, we use an edge coupling scheme where a lensed fiber is aligned to a tapered waveguide (Fig. 2a, b). Light is guided to a reflector and evanescently couples to both an active and a zipper cavity that acts as an experimental control. This control cavity is attached to nanobenders without metallization. The reflection spectrum of the device is recorded for all subsequent measurements (see methods) and the background is removed through normalization (see Supplementary Note 5). The bender-zipper cavity is positioned such that the nanobenders are parallel to the crystal X axis, necessary for the nanobenders to operate as designed. We also fabricate and measure a device with nanobenders perpendicular to the crystal X axis and measure two orders of magnitude lower tuning (see Supplementary Note 6). We attach the nanobenders to the zipper cavity with and without narrow tethers and measure larger tuning

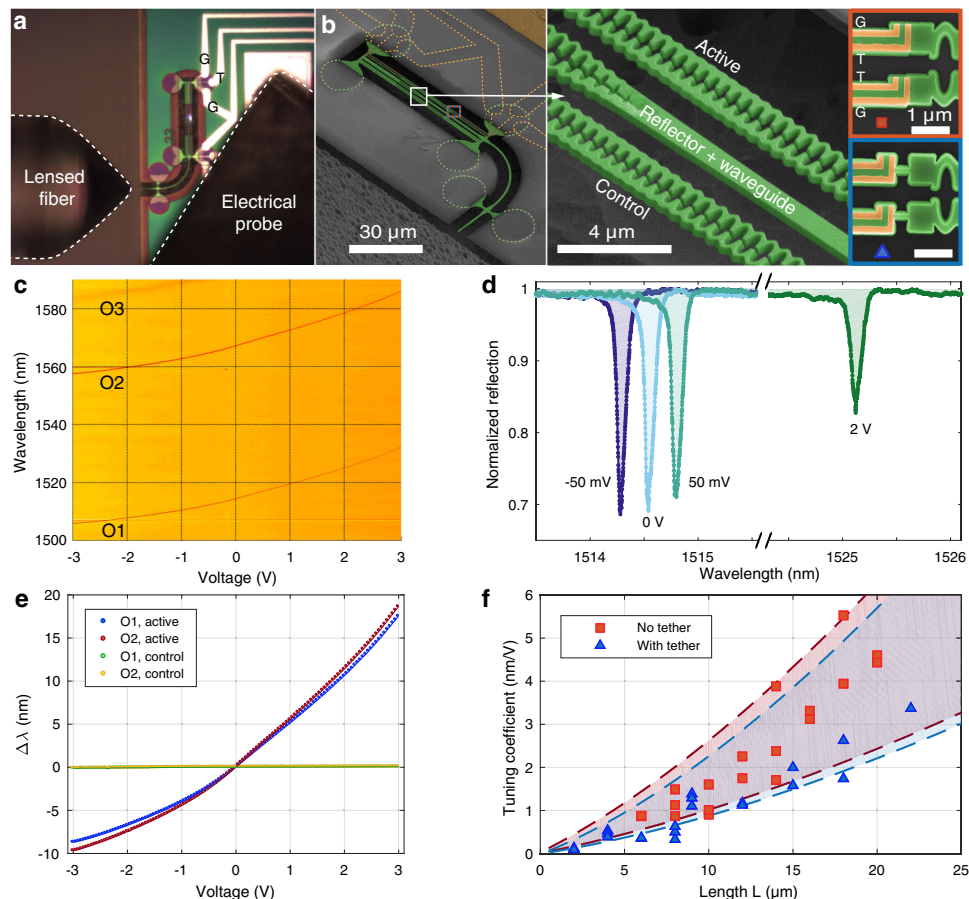


Fig. 2 DC tuning of a bender-zipper cavity. **a** Optical microscope image showing second harmonic generation happening in the zipper cavity as well as the coupling fiber and electrical probe tip. **b** False color scanning electron micrographs of the entire device, the waveguide-zipper coupling region and nanobenders attached to the zipper cavity with (blue triangle) and without tether (red square). **c** Measured DC tuning of three optical modes of a single zipper cavity attached to four $L = 15 \mu\text{m}$ nanobenders through narrow tethers. **d** Selected cut-lines from Fig. 2c at -50 mV , 0 V , 50 mV and 2 V for the fundamental optical mode O_1 . **e** Wavelength tuning as a function of voltage for two modes of the active and control devices. The data are extracted from Fig. 2c. **f** Measured tuning coefficient versus nanobender length L . Error bars are smaller than the marker size in the plot. The dashed lines correspond to simulations with initial gaps of 108 and 258 nm .

in the untethered devices (highlighted in blue and red in Fig. 2b). The motivation and effect of adding the tether is discussed in more detail in Supplementary Note 4. To apply a voltage to the nanobenders, we use electrical probes to make contact with on-chip aluminum pads.

We apply voltages to the nanobenders in steps of 50 mV and obtain the reflection spectrum for each voltage (Fig. 2c). We observe wavelength tuning for three different optical modes O_i of the active cavity. No tuning for the control cavity is observed. Additionally the linear wavelength–voltage relationship around 0 V indicates that tuning originates from the piezoelectric effect, in contrast to electrostatic, thermo-optical, and thermo-mechanical tuning. Reflection spectra near the fundamental optical mode O_1 around 0 V and at 2 V are shown in Fig. 2d. The linewidth of O_1 is around 90 pm corresponding to a quality factor Q of 1.7×10^4 . The linewidth is limited by thermal mechanical broadening and decreases by almost an order of magnitude at 4 K (Supplementary Note 7). The shallower dip at 2 V is due to a decrease of the external coupling rate κ_e as the separation between the zipper cavity and the coupling waveguide is increased by actuation of the nanobender. It may be possible to compensate for this effect by using a secondary nanobender on the coupling waveguide or actuate the two halves of the zipper cavity independently. In Fig. 2e we show the extracted resonance wavelength shift versus DC voltage for O_1 and O_2 of the active

zipper cavity. We can tune over tens of nanometers with CMOS-level voltages, corresponding to hundreds of optical linewidths. We perform a linear fit on this tuning curve for small voltages ($|U| < 0.5 \text{ V}$) and obtain a tuning coefficient quantifying the change in wavelength per volt of 5 nm V^{-1} . All tuning coefficients are reported at 0 V .

We also investigate how tuning coefficient scales with nanobender length (Fig. 2f). For this purpose we fix all other parameters within fabrication imperfections which mostly affect \tilde{g}_0 . More than 40 devices with different L are measured. As expected, the zipper cavities with longer nanobenders tune more. The tuning coefficients are higher on devices without the tethers. This is partly supported by simulations. Hence optimizing the way nanobenders are attached is important for composite mechanical systems.

Modulation speed of the bender-zipper cavity. In addition to slowly tuning the bender-zipper cavity using a DC voltage, we also apply a small AC voltage. This allows us to learn about the AC modulation strength as well as the mechanical resonance frequencies of the bender-zipper device. As shown in Fig. 3a, the total voltage applied on the nanobenders is $V_{dc} + V_{ac} \sin(\Omega t)$ where Ω is the modulation frequency. These voltages lead to wavelength shifts of the cavity given by $\Delta\lambda_{dc} + \Delta\lambda_{ac}(\Omega) \sin(\Omega t + \phi)$ where ϕ is a phase offset. In the DC measurements, we sweep the laser

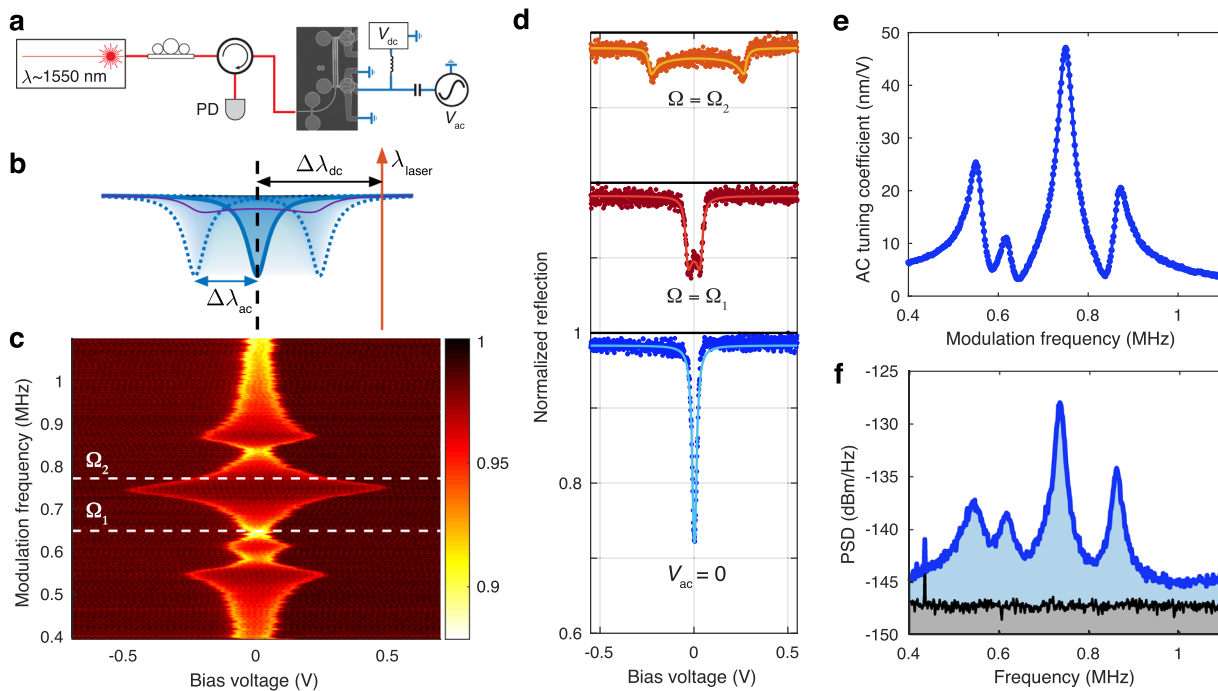


Fig. 3 AC modulation of a bender-zipper cavity. **a** Experimental setup: Light from a tunable laser is sent to the device after passing through a polarization controller and a circulator. The reflected light is measured using a photodetector. DC and AC voltages are applied to the nanobenders via electrical probes. **b** Measurement principle: as the mode is being modulated at frequency Ω , its resonance wavelength is swept across a laser of fixed wavelength by changing the bias voltage. This results in a measurement of the purple curve. **c** Measurement results for a modulation voltage of 50 mV on a bender-zipper cavity with $L = 15 \mu\text{m}$, showing an enhanced response for certain modulation frequencies. **d** Selected cut-lines of Fig. 3c close to resonance, off-resonance and with no modulation. The solid line is an analytical fit of the data. **e** AC tuning coefficient as a function of modulation frequency. It is extracted from fitting Fig. 3c and converting bias voltage to wavelength using the DC tuning coefficient. **f** Thermal-mechanical power spectral density (PSD) of the bender-zipper cavity. For the blue curve, the laser wavelength is close to the optical resonance, for the black curve it is far detuned.

wavelength across the resonance of the cavity. For AC measurements, we instead fix the wavelength of the laser and sweep the cavity using the bias voltage (see Fig. 3b), while using the AC voltage to modulate the cavity resonance. The measurement result is the convolution of the cavity's Lorentzian lineshape with the probability distribution that samples the sinusoidally modulated cavity center frequency.

Sweeping the modulation frequency (Fig. 3c), we observe that the AC tuning coefficient $\alpha_{\text{ac}} \equiv \Delta\lambda_{\text{ac}}/V_{\text{ac}}$ is enhanced at certain frequencies close to 1 MHz. These correspond to the mechanical resonances of the bender-zipper device (Supplementary Note 8). The data were taken with $V_{\text{ac}} = 50$ mV. Cut-lines of the dataset are shown in Fig. 3d, both off-resonance (Ω_1) and close to resonance (Ω_2). We also show a measurement without AC modulation where we recover a simple Lorentzian. We fit the reflection spectra to extract the AC tuning coefficient and plot it as a function of the modulation frequency (Fig. 3e). Consequently, we are not only able to observe the mechanical resonance frequencies of the system but also directly extract the strength of the modulation. On mechanical resonance, the tuning coefficient is enhanced by a factor ~ 10 , amounting to $\alpha_{\text{ac}} \sim 50 \text{ nm V}^{-1}$. This corresponds to $V_{\pi} = \kappa/(2\alpha_{\text{ac}}) \sim 1 \text{ mV}$. As expected, the frequency dependence of the AC tuning coefficient closely matches with the thermal-mechanical spectrum (Fig. 3f). We obtain the thermal-mechanical spectrum by detuning the laser from the cavity by around half a linewidth where the cavity frequency fluctuations are transduced to intensity fluctuations that we detect with a high-speed detector and record on a real-time spectrum analyzer. The mechanical quality factor $Q_m \approx 20$ is relatively low due to air damping. This is verified by measurements in low pressure conditions which show several orders of magnitude enhancement

in Q_m (Supplementary Note 7). Thus, modulation experiments at low pressures could enable even larger resonant AC tuning coefficients (over a smaller bandwidth), reducing V_{π} to $\sim 20 \mu\text{V}$.

Mechanical contact and hysteresis. We have shown that tens of millivolts are sufficient to tune the optical cavity by more than its linewidth. The small gap and large displacement per volt, taken together, means that the two halves of the zipper touch for voltages on the order of 5 V.

We demonstrate continuous wavelength tuning of a bender-zipper cavity with $L = 22 \mu\text{m}$ by reducing the gap between the two halves of the zipper down to the point when they come into contact (Fig. 4a). Focusing on the fundamental mode O_1 , we measure a tuning range of 63 nm with 4.5 V. To the best of our knowledge, this is the largest tuning range demonstrated for an on-chip optical cavity using CMOS-level voltages. From the initial gap size, we infer a displacement actuation of $\sim 25 \text{ nm V}^{-1}$ from each pair of nanobenders. After the contact, the tuning stops regardless of increasing voltage.

As we begin decreasing the voltage, the resonance wavelength shifts ten times less than before the contact because the zipper halves are stuck. We find that the voltage needs to be reduced lower than the contact voltage for the tuning to be restored. This hysteresis is likely due to the van der Waals force that keeps the zippers attached. When we further decrease the voltage, the nanobenders exert a force opposite in direction which eventually manage to detach the zippers. The whole process is reversible as the mode recovers its original wavelength after detaching.

The hysteresis behavior could be applied as an optical memory³⁴ which necessitates hysteresis for functioning. We

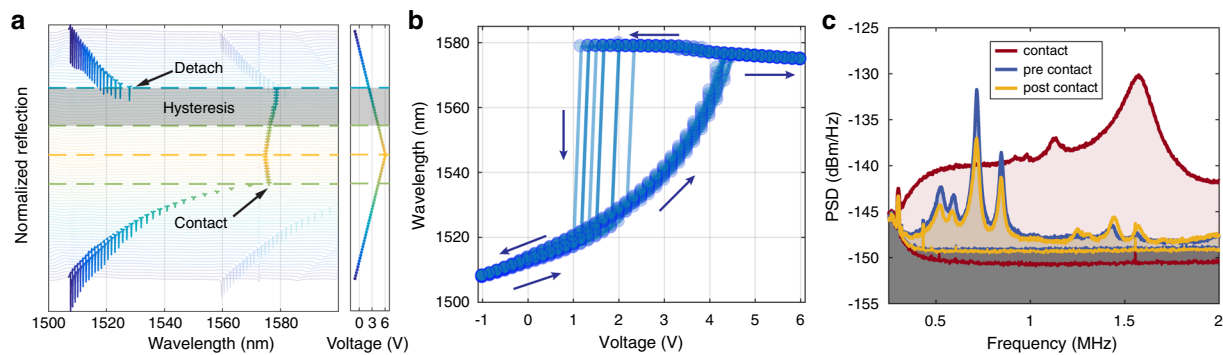


Fig. 4 Mechanical contact of a bender-zipper cavity. **a** One cycle of contact and release of both halves of a zipper cavity attached to $L = 22 \mu\text{m}$ nanobenders via tethers. As the voltage increases from -1 V to 4.5 V in steps of 166 mV , the resonance wavelength of the zipper cavity tunes up from 1508 nm to 1576 nm until both halves of the bender-zipper cavity collide (green dashed line). Further increasing the voltage up to 6 V (yellow dashed line) only has a small effect. Decreasing the voltage, we observe hysteresis (gray region). The blue dashed line indicates where the zipper detaches. $L = 22 \mu\text{m}$ and $\bar{g}_0 = 210\text{ nm}$ (measured on a scanning electron micrograph, pre-release). **b** Repeating nine cycles of contact and release of a zipper cavity revealing a hysteresis loop. **c** Thermal power spectral density (PSD) at different stages of a cycle. The mode structure changes when the zippers are making contact.

test the reliability of the hysteresis loop by repeating the contact-detach process. In Fig. 4b we show nine successive contact-detach cycles, which were preceded by ~ 40 cycles. The hysteresis loop is apparent and there is relatively good overlap between the cycles. However, the voltage at which the zippers detach is not consistent across cycles and drifts to lower voltages. After several cycles, the nanobenders are not able to get the zippers to detach (not shown here) although we have found that applying a short AC pulse on mechanical resonance is able to detach them reliably, acting as a reset operation. After the reset, for several cycles the zippers are again able to detach with a DC voltage. The reason for this behavior will be subject to future investigations.

In Fig. 4c we show measurements of the thermal power spectral density of the bender-zipper cavity before contact, during contact and after detaching. We see a clear difference in the spectra between the detached zipper and the attached one. In the latter case, the lateral relative motion between the two halves of the zipper cavity is effectively suppressed. The higher noise floor measured during the contact is likely from laser phase noise, which is more efficiently transduced due to a narrower optical linewidth. We are thus able to reversibly modify both the optical and mechanical properties of the zipper cavity using the nanobenders.

Discussion

Beyond the demonstrated tunable bender-zipper nanophotonic cavity, various tunable nanophotonic components including phase shifters and couplers can be realized with nanobenders. We show some examples in Fig. 5a-e. An array of nanobenders connected in parallel to a sliced ridge waveguide acts as a phase shifter. The two halves of the sliced ridge waveguide shift towards or away from each other, effectively tuning the index of the fundamental transverse electric mode^{4,11}.

For applications where a large displacement per volt is desired, a series of nanobenders could be connected in a zig-zag fashion to reduce the length of the occupied region. The direction of the actuated displacement can be controlled by engineering the aspect ratio of the zig-zag pattern (Supplementary Note 9). We show one zig-zag bender with four $L = 15 \mu\text{m}$ nanobenders and one with twenty $L = 4 \mu\text{m}$ nanobenders (Fig. 5b, c). They have similar simulated displacement per volt of $\sim 50 \text{ nm V}^{-1}$ and actuated along two different directions.

Until now, we have considered nanobenders fabricated with Y-cut LiNbO₃, where the dominant displacement is in-plane, parallel to the surface of the chip. Nanobenders with identical geometry fabricated on Z-cut LiNbO₃ and parallel to the crystal X axis, would generate vertical bending (Supplementary Note 1 & 2). As shown in Fig. 5d, these nanobenders can be connected in parallel, for extra structural support, and used to implement a tunable optical coupler^{9,10}. Moreover, when connected in a zig-zag fashion, a twist is accumulated along the zig-zag. This can be applied to tilt a mirror attached to the end of the zig-zag structure (Fig. 5e). The rotation angle per volt, actuation speed and device footprint of this type of piezoelectric micro-mirror are comparable to those of the widely used Digital Mirror Devices³⁵.

To summarize, we have introduced and implemented the nanobender, a component capable of generating tens of nanometers of displacement per volt using the piezoelectric effect at the submicron scale. We have experimentally shown tuning of a photonic resonator over the entire telecom C-band with CMOS-level voltages and proposed several new photonic devices that leverage the capabilities of the nanobender. Greater control over photonic and phononic devices on the promising thin-film lithium niobate material platform complements on-going efforts to implement ultra-low-power modulation^{36,37}, nonlinear nanophotonic circuits^{38–40}, quantum nanomechanics^{41,42}, and microwave optomechanical transduction^{43–46}. For emerging quantum technologies that require frequency matching nanophotonic cavities to quantum dots, color centers or rare-earth-doped crystals^{47–49}, our approach benefits from being able to operate at cryogenic temperatures, while avoiding electric fields, excess carriers, and adsorbed gas molecules, all of which have deleterious effects on the cavity or emitter. Finally, the linear voltage-displacement nature of the piezoelectric effect, the ability to engineer the frequency response and the possibility of dense integration with full electrical access make the nanobenders appealing for sensing^{15,50–52} and energy harvesting^{53,54}.

Methods

Device fabrication. We start with $t \approx 500\text{ nm}$ thin-film LiNbO₃ on a $\sim 500 \mu\text{m}$ thick silicon substrate. Thickness of the LiNbO₃ layer is measured through ellipsometry. The LiNbO₃ is first thinned to $t = 300\text{ nm}$ through blanket argon ion milling. We then pattern the LiNbO₃ using electron beam lithography (EBL) by coating the sample with hydrogen silsesquioxane (HSQ), a negative electron beam resist (Dow Corning, FOX-16). A 10 nm Ti adhesion layer between the LiNbO₃ and HSQ is evaporated prior to the spin coat. The exposure is followed by a development of the HSQ using 25% tetramethylammonium hydroxide and an electron beam hardening step⁵⁵. The pattern is then transferred to LiNbO₃ by argon ion

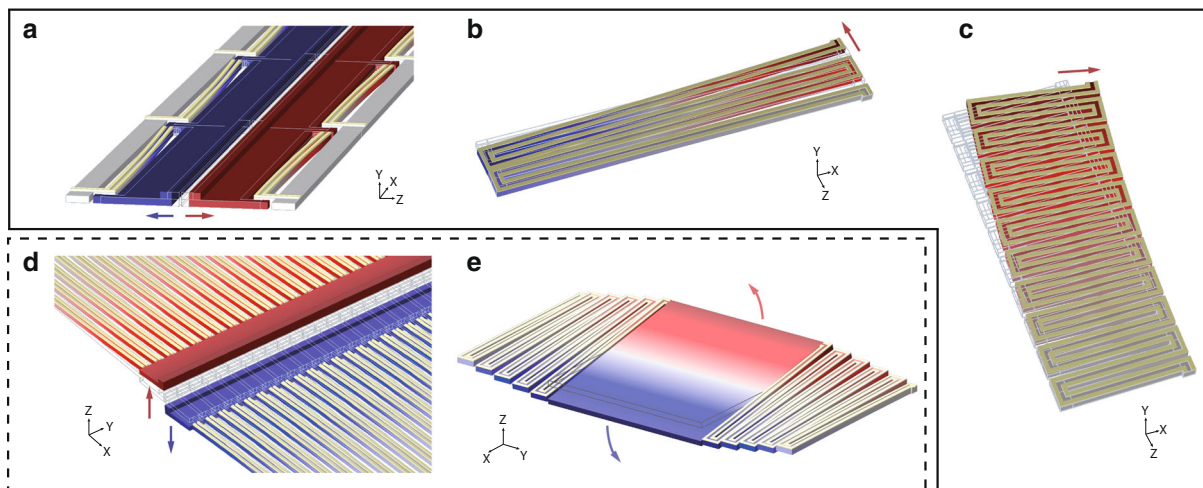


Fig. 5 Outlook for nanobenders. Simulated displacement is shown with the metal electrodes colored in bright yellow and lithium niobate colored with relevant displacement field. Directions of the displacements are indicated by colored arrows. The undeformed geometries are outlined in gray. **a** Attaching a sliced ridge waveguide to an array of in-plane nanobenders on Y-cut LiNbO₃. The sliced ridge waveguide could operate as either a tunable phase shifter or a tunable coupler. **b, c** On nanobenders connected in series in a zig-zag fashion, the displacement accumulates and can be actuated along different directions by engineering the aspect ratio of the zig-zag pattern. **d** Nanobenders connected in parallel on Z-cut LiNbO₃. A similar non-uniform E field generates out-of-plane bending. A tunable optical coupler can be realized. **e** Z-cut nanobenders connected in a zig-zag pattern. An out-of-plane twist accumulates along the zig-zag structure and can be utilized to tilt a nanophotonic mirror or diffraction grating (not shown in detail).

milling the LiNbO₃ not covered by HSQ. We proceed with stripping the leftover HSQ with buffered oxide etch and doing an acid clean with diluted hydrofluoric acid to remove re-deposited amorphous LiNbO₃⁵⁶. A second aligned EBL step patterns the liftoff mask for the submicron electrodes on the nanobenders, this time using a positive resist (Allresist, AR-P 6200.13). Aluminum of thickness $t_m = 50$ nm is evaporated and lifted off using N-Methyl Pyrrolidone (MicroChem, Remover PG). To pattern the electric probe pads and the wires connecting them to the submicron electrodes, we use photolithography, and subsequent 250 nm aluminum evaporation and liftoff. Because the probes pads are sitting on the silicon substrate, the two evaporated aluminum layers overlap at the edge of the 300 nm LiNbO₃ film. The edges of the chip are diced to expose the tapered optical couplers. Finally we do a masked release of the LiNbO₃ using XeF₂ which selectively etches the silicon. Sometimes both halves of the zipper cavity are stuck together after release. We notice that using a scanning electron microscope to charge up the structures can get them unstuck.

Optical characterization. All the measurements are done on reflection and a simplified setup is drawn in Fig. 3a. A tunable telecom laser (Velocity TLB-6700 and alternatively sancet TSL-550) injects light into an optical fiber. With the help of a variable optical attenuator we can control the optical power. Before reaching the tip of a lensed fiber, the light goes through a polarization controller as well as a circulator (port 1 → 2). The lensed fiber is then aligned with the on-chip edge coupler by maximizing the reflection signal from the on-chip reflector. The typical fiber-to-chip coupling efficiency is $\eta \sim 50\%$. The reflected signal goes back through the circulator (port 2 → 3) and is lead to a photodetector (Newport model 1623). By sweeping the laser wavelength, we directly see the modes as dips in the reflection spectrum. To directly identify the optical modes, we can make use of the optical nonlinearity of LiNbO₃. For high optical powers ($\sim 200 \mu\text{W}$), we observe second harmonic generation happening inside the cavity using a simple optical microscope and a CMOS camera. This is due to the cavity not being resonant around wavelengths of 775 nm so that light radiates to free space. This can help us identify the optical mode and tell us if it is located in the control or active zipper cavity. Furthermore, when measuring the thermal-mechanical power spectral density of the zipper cavity, the wavelength of the laser is slightly detuned from an optical resonance. Instead of going to the photodetector, reflected light is first sent to an erbium-doped fiber amplifier (EDFA) and subsequently to a high-speed photodetector (Newport model 1554-B). We then measure the mechanical spectrum with a real-time spectrum analyzer (Rohde & Schwarz FSW).

Extracting the AC tuning coefficient. The AC voltage is generated using a signal generator (Rigol DG4102) and combined in a bias tee with the DC voltage. It is applied to the on-chip aluminum pads through a micromanipulator (MiSUMi XYZLNG25) and electrical probes (GGB Industries, Picoprobe model 40A-GSG), or alternatively wire bonding. Considering strong modulation $\Delta\omega_{\text{dc}} + \Delta\omega_{\text{ac}} \cos(\Omega t)$ where $\Delta\omega_{\text{dc}}$ is the detuning from the mode with no modulation and

$\Delta\omega_{\text{ac}}$ the modulation amplitude. This leads to a time-averaged optical reflection signal $|r|^2|$ described by

$$|r|^2 = 1 - \frac{c}{2b} \left(\frac{1}{\sqrt{1 - (a - ib)^2}} + \frac{1}{\sqrt{1 - (a + ib)^2}} \right), \quad (2)$$

where $a \equiv \Delta\omega_{\text{dc}}/\Delta\omega_{\text{ac}}$, $b \equiv \kappa/(2\Delta\omega_{\text{ac}})$, and $c \equiv (\kappa\kappa_e - \kappa_e^2)/\Delta\omega_{\text{ac}}^2 \cdot \Delta\omega_{\text{ac}}$ and $\kappa\kappa_e - \kappa_e^2$ are the two fitting parameters. Qualitatively, we understand the shape of the curve by noticing that the mode spends more time around the extrema of the sinusoidal modulation, hence two peaks form symmetrically with respect to the original cavity resonance. On the other hand, the mode spends the least amount of time at the center as this is where the slope of the sine function is largest. Additionally, because the laser is fixed in the measurement, the small but complicated wavelength-dependent background fluctuations of the measurement setup are no longer present which facilitates faithful fitting of the curve to extract the AC tuning coefficient.

Data availability

All data that support the findings of this study are available in the main text, Supplementary Information, as well as from the corresponding authors upon reasonable request.

Received: 8 June 2020; Accepted: 16 July 2020;

Published online: 04 September 2020

References

- Miller, D. A. Attojoule optoelectronics for low-energy information processing and communications. *J. Lightwave Technol.* **35**, 346–396 (2017).
- Hamerly, R., Bernstein, L., Sludds, A., Soljačić, M. & Englund, D. Large-scale optical neural networks based on photoelectric multiplication. *Phys. Rev. X* **9**, 021032 (2019).
- Pai, S., et al. Parallel programming of an arbitrary feedforward photonic network. *IEEE J. Sel. Top. Quantum Electron.* **26**, 6100813 (2020).
- Midolo, L., Schliesser, A. & Fiore, A. Nano-opto-electro-mechanical systems. *Nat. Nanotechnol.* **13**, 11–18 (2018).
- Safavi-Naeini, A. H., Van Thourhout, D., Baets, R. & Van Laer, R. Controlling phonons and photons at the wavelength scale: integrated photonics meets integrated phononics. *Optica* **6**, 213–232 (2019).
- Zheludev, N. I. & Plum, E. Reconfigurable nanomechanical photonic metamaterials. *Nat. Nanotechnol.* **11**, 16–22 (2016).
- Wu, M. C., Solgaard, O. & Ford, J. E. Optical MEMS for lightwave communication. *J. Lightwave Technol.* **24**, 4433–4454 (2006).

8. Van Acocleyen, K. et al. Ultracompact phase modulator based on a cascade of NEMS-operated slot waveguides fabricated in silicon-on-insulator. *IEEE Photon. J.* **4**, 779–788 (2012).
9. Han, S., Seok, T. J., Quack, N., Yoo, B.-W. & Wu, M. C. Large-scale silicon photonic switches with movable directional couplers. *Optica* **2**, 370–375 (2015).
10. Seok, T. J., Quack, N., Han, S., Muller, R. S. & Wu, M. C. Large-scale broadband digital silicon photonic switches with vertical adiabatic couplers. *Optica* **3**, 64–70 (2016).
11. Papon, C. et al. Nanomechanical single-photon routing. *Optica* **6**, 524–530 (2019).
12. Haffner, C. et al. Nano - opto-electro-mechanical switches operated at CMOS-level voltages. *Science* **864**, 860–864 (2019).
13. Perahia, R., Cohen, J., Meenehan, S., Alegre, T. M. & Painter, O. Electrostatically tunable optomechanical "zipper" cavity laser. *Appl. Phys. Lett.* **97**, 191112 (2010).
14. Winger, M. et al. A chip-scale integrated cavity-electro-optomechanics platform. *Opt. Express* **19**, 24905–24921 (2011).
15. Bagci, T. et al. Optical detection of radio waves through a nanomechanical transducer. *Nature* **507**, 81–85 (2014).
16. Andrews, R. W. et al. Bidirectional and efficient conversion between microwave and optical light. *Nat. Phys.* **10**, 321–326 (2014).
17. Pitanti, A. et al. Strong opto-electro-mechanical coupling in a silicon photonic crystal cavity. *Opt. Express* **23**, 3196–3208 (2015).
18. Grutter, K. E., Davanco, M. I., Balram, K. C. & Srinivasan, K. Invited article: Tuning and stabilization of optomechanical crystal cavities through NEMS integration. *APL Photonics* **3**, 100801 (2018).
19. Bekker, C. et al. Free spectral range electrical tuning of a high quality on-chip microcavity. *Opt. Express* **26**, 33649–33670 (2018).
20. Hosseini, N. et al. Stress-optic modulator in TriPleX platform using a piezoelectric lead zirconate titanate (PZT) thin film. *Opt. Express* **23**, 14018–14026 (2015).
21. Tian, H., Dong, B., Zervas, M., Kippenberg, T. J. & Bhave, S. A. An unreleased MEMS actuated silicon nitride resonator with bidirectional tuning. In *CLEO: Science and Innovations SW4B-3* (Optical Society of America, 2018).
22. Jin, W., Polcawich, R. G., Morton, P. A. & Bowers, J. E. Piezoelectrically tuned silicon nitride ring resonator. *Opt. Express* **26**, 3174–3187 (2018).
23. Stanfield, P., Leenheer, A., Michael, C., Sims, R. & Eichenfield, M. CMOS-compatible, piezo-optomechanically tunable photonics for visible wavelengths and cryogenic temperatures. *Opt. Express* **27**, 28588–28605 (2019).
24. Eichenfield, M., Camacho, R., Chan, J., Vahala, K. J. & Painter, O. A picogram-and nanometre-scale photonic-crystal optomechanical cavity. *Nature* **459**, 550–555 (2009).
25. Leijssen, R. & Verhagen, E. Strong optomechanical interactions in a sliced photonic crystal nanobeam. *Sci. Rep.* **5**, 15974 (2015).
26. Weis, R. & Gaylord, T. Lithium niobate: summary of physical properties and crystal structure. *Appl. Phys. A* **37**, 191–203 (1985).
27. Guy, I., Muensit, S. & Goldys, E. Extensional piezoelectric coefficients of gallium nitride and aluminum nitride. *Appl. Phys. Lett.* **75**, 4133–4135 (1999).
28. COMSOL AB. COMSOL Multiphysics v. 5.4. <https://www.comsol.com>.
29. Safari, A. & Akdogan, E. K. *Piezoelectric and Acoustic Materials for Transducer Applications* (Springer Science & Business Media, 2008).
30. Baek, S. et al. Giant piezoelectricity on Si for hyperactive MEMS. *Science* **334**, 958–961 (2011).
31. Conrad, H. et al. A small-gap electrostatic micro-actuator for large deflections. *Nat. Commun.* **6**, 10078 (2015).
32. Zubko, P., Catalan, G. & Tagantsev, A. K. Flexoelectric effect in solids. *Annu. Rev. Mater. Sci.* **43**, 387–421 (2013).
33. Bhaskar, U. K. et al. A flexoelectric microelectromechanical system on silicon. *Nat. Nanotechnol.* **11**, 263–266 (2016).
34. Bagheri, M., Poot, M., Li, M., Pernice, W. P. & Tang, H. X. Dynamic manipulation of nanomechanical resonators in the high-amplitude regime and non-volatile mechanical memory operation. *Nat. Nanotechnol.* **6**, 726–732 (2011).
35. Dudley, D., Duncan, W. M. & Slaughter, J. in *MOEMS Display and Imaging Systems* vol. 4985, 14–25 (International Society for Optics and Photonics, 2003).
36. Wang, C. et al. Integrated lithium niobate electro-optic modulators operating at CMOS-compatible voltages. *Nature* **562**, 101–104 (2018).
37. Zhang, M. et al. Broadband electro-optic frequency comb generation in a lithium niobate microring resonator. *Nature* **568**, 373–377 (2019).
38. Wang, C. et al. Ultrahigh-efficiency wavelength conversion in nanophotonic periodically poled lithium niobate waveguides. *Optica* **5**, 1438–1441 (2018).
39. Chen, J.-Y. et al. Ultra-efficient frequency conversion in quasi-phase-matched lithium niobate microrings. *Optica* **6**, 1244–1245 (2019).
40. Lu, J. et al. Periodically poled thin-film lithium niobate microring resonators with a second-harmonic generation efficiency of 250,000%/W. *Optica* **6**, 1455–1460 (2019).
41. Arrangoiz-Arriola, P. et al. Coupling a superconducting quantum circuit to a phononic crystal defect cavity. *Phys. Rev. X* **8**, 031007 (2018).
42. Arrangoiz-Arriola, P. et al. Resolving the energy levels of a nanomechanical oscillator. *Nature* **571**, 537–540 (2019).
43. Jiang, W. et al. Lithium niobate piezo-optomechanical crystals. *Optica* **6**, 845–853 (2019).
44. Shao, L. et al. Microwave-to-optical conversion using lithium niobate thin-film acoustic resonators. *Optica* **6**, 1498–1505 (2019).
45. Dahmani, Y. D., Sarabalis, C. J., Jiang, W., Mayor, F. M. & Safavi-Naeini, A. H. Piezoelectric transduction of a wavelength-scale mechanical waveguide. *Phys. Rev. Appl.* **13**, 024069 (2020).
46. Jiang, W. et al. Efficient bidirectional piezo-optomechanical transduction between microwave and optical frequency. *Nat. Commun.* **11**, 1–7 (2020).
47. Englund, D. et al. Controlling the spontaneous emission rate of single quantum dots in a two-dimensional photonic crystal. *Phys. Rev. Lett.* **95**, 013904 (2005).
48. Faraon, A., Barclay, P. E., Santori, C., Fu, K.-M. C. & Beausoleil, R. G. Resonant enhancement of the zero-phonon emission from a colour centre in a diamond cavity. *Nat. Photonics* **5**, 301–305 (2011).
49. Zhong, T., Kindem, J. M., Miyazono, E. & Faraon, A. Nanophotonic coherent light-matter interfaces based on rare-earth-doped crystals. *Nat. Commun.* **6**, 8206 (2015).
50. Arlett, J. L., Myers, E. B. & Roukes, M. L. Comparative advantages of mechanical biosensors. *Nat. Nanotechnol.* **6**, 203–215 (2011).
51. Krause, A. G., Winger, M., Blasius, T. D., Lin, Q. & Painter, O. A high-resolution microchip optomechanical accelerometer. *Nat. Photonics* **6**, 768–772 (2012).
52. Mason, D., Chen, J., Rossi, M., Tsaturyan, Y. & Schliesser, A. Continuous force and displacement measurement below the standard quantum limit. *Nat. Phys.* **15**, 745–749 (2019).
53. Wang, Z. L. & Song, J. Piezoelectric nanogenerators based on zinc oxide nanowire arrays. *Science* **312**, 242–246 (2006).
54. Wang, Z. L. Towards self-powered nanosystems: from nanogenerators to nanopiezotronics. *Adv. Funct. Mater.* **18**, 3553–3567 (2008).
55. Yang, J. K., Anant, V. & Berggren, K. K. Enhancing etch resistance of hydrogen silsesquioxane via postdevelop electron curing. *J. Vac. Sci. Technol. B* **24**, 3157–3161 (2006).
56. Hartung, H. et al. Fabrication of ridge waveguides in zinc-substituted lithium niobate by means of ion-beam enhanced etching. *Opt. Lett.* **33**, 2320–2322 (2008).

Acknowledgements

W.J. and F.M.M. would like to thank Agnetta Y. Cleland, E. Alex Wollack, Jeremy D. Witmer, Patricio Arrangoiz-Arriola, and Raphaël Van Laer for helpful discussions. We thank Chris Rogers for technical support. This work was supported by the David and Lucile Packard Fellowship, the Stanford University Terman Fellowship and by the U.S. government through the National Science Foundation (NSF) (1708734, 1808100), Air-force Office of Scientific Research (AFOSR) (MURI No. FA9550-17-1-0002 led by CUNY). R.N.P. is partly supported by the NSF Graduate Research Fellowships Program (DGE-1656518). The authors wish to thank NTT Research Inc. for their financial and technical support. Device fabrication was performed at the Stanford Nano Shared Facilities (SNSF) and the Stanford Nanofabrication Facility (SNF). SNSF is supported by the National Science Foundation under award ECCS-1542152.

Author contributions

W.J. and A.H.S.-N. conceived the project. W.J. and F.M.M. designed and fabricated the devices. W.J., F.M.M., and T.P.M. developed the fabrication process. F.M.M. and W.J. conducted the measurements with assistance from R.N.P. and C.J.S., F.M.M. and W.J. wrote the manuscript with input from all authors. A.H.S.-N. supervised the project.

Competing interests

A.H.S.-N., W.J., F.M.M., and R.N.P. have filed a provisional patent application 62/935953 about the contents of this manuscript. The remaining authors declare no competing interests.

Additional information

Supplementary information is available for this paper at <https://doi.org/10.1038/s42005-020-00412-3>.

Correspondence and requests for materials should be addressed to A.H.S.-N.

Reprints and permission information is available at <http://www.nature.com/reprints>

Publisher's note Springer Nature remains neutral with regard to jurisdictional claims in published maps and institutional affiliations.



Open Access This article is licensed under a Creative Commons Attribution 4.0 International License, which permits use, sharing, adaptation, distribution and reproduction in any medium or format, as long as you give appropriate credit to the original author(s) and the source, provide a link to the Creative Commons license, and indicate if changes were made. The images or other third party material in this article are included in the article's Creative Commons license, unless indicated otherwise in a credit line to the material. If material is not included in the article's Creative Commons license and your intended use is not permitted by statutory regulation or exceeds the permitted use, you will need to obtain permission directly from the copyright holder. To view a copy of this license, visit <http://creativecommons.org/licenses/by/4.0/>.

© The Author(s) 2020